nature portfolio

https://doi.org/10.1038/s41586-021-04012-1

Supplementary information

Optomechanical dissipative solitons

In the format provided by the authors and unedited

Supplementary Information:

Optomechanical Dissipative Solitons

Jing Zhang[1,2], Bo Peng[1], Seunghwi Kim[3], Faraz Monifi[1], Xuefeng Jiang[1], Yihang Li[1], Peng Yu[4], Lianqing Liu[4], Yu-xi Liu[5], Andrea Alù[3,6], and Lan Yang[1*]

Affiliations:

[1]Department of Electrical and Systems Engineering, Washington University, St. Louis, MO 63130, USA

[2]Department of Automation, Tsinghua University, Beijing 100084, P. R. China

[3]Photonics Initiative, Advanced Science Research Center, City University of New York, New York, NY 10031, USA

[4]State Key Laboratory of Robotics, Shenyang Institute of Automation, CAS, Shenyang 110016, P. R. China

[5]Institute of Microelectronics, Tsinghua University, Beijing 100084, P. R. China

[6]Physics Program, Graduate Center, City University of New York, New York, NY 10016, USA

*email: yang@ese.wustl.edu

I. NONLINEAR MECHANICAL TRAVELLING-WAVE EQUATION

The mechanical mode we observe in experiments with frequency $\Omega_m = 27.3\,\mathrm{MHz}$ is a mode that propagates along the radial direction of the microtoroid, i.e., propagating from the edge of the microtoroid to the centre and then reflecting back (see Fig. S1a). When the optical pump power is low but above the threshold of optomechanical oscillations, the effective frequency of the mechanical mode is fixed. Thus, the forward mechanical wave and the backward one superimpose to generate stable standing wave. However, when we increase the optical pump power, the system

will become unstable, and the mechanical traveling wave propagates back and forth across the surface of the microtoroid resonator. Consequently, the standing wave will not be formed anyway. When the mechanical traveling wave arrives at the edge of the microtoroid, the periodic nonlinear modulation from the optical field via the optomechanical interaction leads to nonlinear and dispersive effects of the mechanical traveling wave. The above physical picture is illustrated in Fig. S1b in which the mechanical traveling wave propagates through a virtual lattice with the unit cell composed of the microtoroid resonator and is modulated periodically [S1] that leads to the dispersive and nonlinear effects for the mechanical traveling wave. An equivalent one-dimensional lattice model is given in Fig. 1d. The balanced nonlinear and dispersive effects lead to the stable localized mechanical traveling wave.

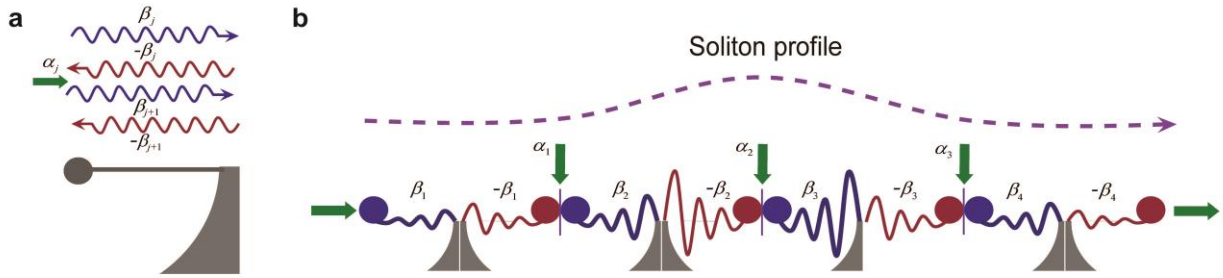

Figure S1. Schematic diagram of the propagation of a mechanical traveling wave in optomechanical resonator. a, The mechanical traveling wave which interacts periodically with the optical mode at the edge of the microtoroid: β_j is the amplitude of the forward and backward mechanical traveling wave for the $j-\text{th}$ round trip, where a $\pi-$phase shift is introduced when the mechanical traveling wave is reflected back from the centre of the microtoroid. α_j is the amplitude of the optical field when the mechanical traveling wave arrives at the edge of the microtoroid after the $j-\text{th}$ round of trip. **b,** The propagation of the mechanical traveling wave through the virtual optomechanical lattice with the unit cell composed of the microtoroid resonator

as shown in **a**, in which the mechanical traveling wave is periodically modulated by the optical field.

To derive the equation of the mechanical traveling wave, let us consider the interaction between the mechanical traveling wave and the optical field shown in Fig. S1. The whole evolution process of the mechanical traveling wave for the $j-\text{th}$ round trip can be decomposed into two stages.

(i) The mechanical traveling wave interacts with the optical field at the edge of the microtoroid after the $(j-1)-\text{th}$ round trip and propagates towards the centre of the microtoroid:

The dynamics of the optical field can be expressed as

$$\dot{\alpha}_{j-1} = -(\gamma + i\Delta)\alpha_{j-1} + ig_{om}(\beta_{j-1} + \beta_{j-1}^{*})\alpha_{j-1} - ig_{om}(\beta_{j} + \beta_{j}^{*})\alpha_{j-1} + i\sqrt{2\gamma_{\text{ext}}}\varepsilon, \quad \text{(S.1)}$$

where $-\beta_{j-1}$ and α_{j-1} are the amplitude of the backward mechanical traveling wave and the amplitude of the optical field after the $(j-1)-\text{th}$ round of trip. β_j is the amplitude of the forward mechanical traveling wave for the $j-\text{th}$ round of trip. Note that a $\pi-$phase shift is introduced to the mechanical traveling wave at the edge of the microtoroid, and therefore the complex amplitude of the backward mechanical mode is given by $-\beta_{j-1}$. $\gamma = \gamma_0 + \gamma_{\text{ext}}$ is the total damping rate of the optical mode. γ_0 is the intrinsic damping rates of the optical mode induced, e.g., by the material absorption, scattering, and radiation. γ_{ext} is the damping rate of the optical mode induced by the coupling between the resonator and the fibre-taper. $\varepsilon(t)$ is the complex amplitude of the external driving field. Δ is the frequency detuning between the input field and the cavity mode. g_{om} is the optomechanical coupling strength.

(ii) The mechanical traveling wave is reflected back from the centre of the microtoroid and interacts with the optical field at the edge of the microtoroid to finish the $j-$th round trip:

The dynamics of the mechanical traveling wave can be denoted as

$$\dot{\beta}_j = -\left(\Gamma_m + i\Omega_m\right)\beta_j - ig_{om}\alpha_{j-1}^{*}\alpha_{j-1} + ig_{om}\alpha_j^{*}\alpha_j. \tag{S.2}$$

The signs of the last two terms are different due to the $\pi-$phase shift introduced when the mechanical traveling wave is reflected back from the centre of the microtoroid. Note that in Eq. (S.2), the non-zero damping rate Γ_m leads to the decay of the mechanical travelling wave, and thus will destroy the stable mechanical wave-packet. This intrinsic loss will be compensated by the mechanical gain provided by optical pumping through the mechanism of phonon lasing. To show this, our experiments are implemented in the unresolved sideband regime and thus the Stokes mode will be involved. The optical mode α_j and the Stokes mode $\alpha_{s,j}$ act as a two-level system, which exchanges energy with the mechanical mode β_j. Taking the continuous limit by setting $R \to 0$, we can combine such a phonon lasing action on β_j from $\alpha_j, \alpha_{s,j}$ and $\alpha_{j-1}, \alpha_{s,j-1}$ together. By omitting the optomechanical coupling terms with coupling strength g_{om} in $\alpha_j, \alpha_{s,j}$ which only induces negligibly small frequency shift for the optical mode and thus do not affect the phonon lasing effects for the mechanical travelling wave, the modified dynamical equation can be expressed as [S2, S3, S4]

$$\dot{\beta}_j = -\left(\Gamma_m + i\Omega_m\right)\beta_j - ig_{om}\alpha_{j-1}^{*}\alpha_{j-1} + ig_{om}\alpha_j^{*}\alpha_j - ig_{om}J_{-,j}, \tag{S.3}$$

$$\dot{J}_{-,j} = -\left(2\gamma - i\Omega_m\right)J_{-,j} + ig_{om}\beta J_{z,j} + \Lambda_{-}, \tag{S.4}$$

$$\dot{J}_{+,j} = -\left(2\gamma + i\Omega_m\right)J_{+,j} - ig_{om}\beta^{*}J_{z,j} + \Lambda_{-}^{*}, \tag{S.5}$$

$$\dot{J}_{z,j} = -2\gamma J_{z,j} + 2ig_{om}\beta^* J_{-,j} - 2ig_{om}\beta J_{+,j} + \Lambda, \tag{S.6}$$

where the laddering operators $J_{\pm,j}$ and $J_{z,j}$ is defined as

$$J_{+,j} = \alpha_j^* \alpha_{s,j}, \qquad J_{-,j} = \alpha_{s,j}^* \alpha_j, \qquad J_{z,j} = \alpha_j^* \alpha_j - \alpha_{s,j}^* \alpha_{s.j}. \tag{S.7}$$

By omitting the nonlinear terms, the incoherent pumping strengths Λ, Λ_- can be calculated by

$$\Lambda = \frac{4\gamma\gamma_{\text{ext}}}{\gamma^2 + \Delta^2}\left|\varepsilon\right|^2, \qquad \Lambda_- = \frac{2\gamma_{\text{ext}}}{\gamma + i\Delta}\left|\varepsilon\right|^2. \tag{S.8}$$

Since $\Gamma_m \ll \gamma$, we can adiabatically eliminate the degrees of freedom of the optical modes, by which the dynamical equation (S.3) can be written as

$$\dot{\beta}_j = -\left[\left(\Gamma_m - G\right) + i\Omega_m\right]\beta_j - \xi\left|\beta_j\right|^2 \beta_j - ig_{om}\alpha_{j-1}^* \alpha_{j-1} + ig_{om}\alpha_j^* \alpha_j, \tag{S.9}$$

where

$$G = \frac{g_{om}^2}{\left(4\gamma^2 + \Omega_m^2\right)}\Lambda \tag{S.10}$$

is the mechanical gain induced by the phonon lasing effects, and

$$\xi = \frac{4g_{om}^4}{\left(4\gamma^2 + \Omega_m^2\right)^2}\Lambda \tag{S.11}$$

is the strength of the third-order nonlinear term induced by optomechanics. Here, we have omitted the mechanical frequency shift induced by optomechaincal coupling which is far-smaller than the mechanical frequency Ω_m. It is shown that the mechanical damping rate is modified as

$$\tilde{\Gamma}_m = \Gamma_m - G. \tag{S.12}$$

It can be seen from Eq. (S.12) that the intrinsic mechanical loss will be completely compensated by the phonon lasing effects when the optical input strength exceed a threshold value

$$\varepsilon_{\text{threshold}}^2 = \frac{\Gamma_m\left(4\gamma^2+\Omega_m^2\right)\left(\gamma^2+\Delta^2\right)}{4\gamma\gamma_{\text{ext}}g_{om}^2}. \tag{S.13}$$

After that, the saturation induced by the higher nonlinear term $-\xi\left|\beta_j\right|^2\beta_j$ and the phonon lasing effects drive the mechanical mode into non-zero stationary state.

The Stokes mode $\alpha_{s,j}$ and the mechanical mode β_j also give a correction term for the dynamical equation of the optical mode α_j, which leads to a stationary effective driving term for α_j. By combing the above processes for the propagation of the mechanical travelling wave, the interaction between the optical field and the mechanical travelling wave can be simplified as the picture given in Fig. S1a and thus can be expressed as the dynamical equations

$$\dot{\alpha}_j = -\left(\gamma+i\Delta\right)\alpha_j + ig_{om}\left(\beta_j+\beta_j^*\right)\alpha_j - ig_{om}\left(\beta_{j+1}+\beta_{j+1}^*\right)\alpha_j + i\sqrt{2\gamma_{\text{ext}}}\varepsilon(t) + i\sqrt{2\gamma_{\text{ext}}}e^{-i\Omega_m t}\tilde{\varepsilon}(t), \tag{S.14}$$

$$\dot{\beta}_j = \left[\left(G-\Gamma_m\right)-\xi\left|\beta_j\right|^2 - i\Omega_m\right]\beta_j - ig_{om}\alpha_{j-1}^*\alpha_{j-1} + ig_{om}\alpha_j^*\alpha_j, \tag{S.15}$$

where

$$\tilde{\varepsilon}(t) = \frac{g_{om}^2\gamma_{\text{ext}}\left(-\gamma^2+i\gamma\Delta\right)\left|\varepsilon(t)\right|^2\varepsilon(t)}{\gamma\Gamma_m\left(\gamma^2+\Delta^2\right)\left[\gamma^2+\left(\Delta-\Omega_m\right)^2\right]}. \tag{S.16}$$

Since the output optical field and the mechanical mode oscillate with the modulation frequency of Ω_m, we can assume that $\alpha_j(t) = \tilde{\alpha}_{j0}(t) + e^{-i\Omega_m t}\tilde{\alpha}_j(t)$ and $\beta_j(t) = \tilde{\beta}_{j0}(t) + e^{-i\Omega_m t}\tilde{\beta}_j(t)$, where $\tilde{\alpha}_{j0}(t)$ and $\tilde{\beta}_{j0}(t)$ represent the baselines of the output optical field and the mechanical mode, and $\tilde{\alpha}_j(t)$ and $\tilde{\beta}_j(t)$ are the slow-varying envelops of the output optical field and the mechanical

mode. Since the evolution time scales of the baselines and the slow-varying envelops are much larger than $\tau = 1/\gamma$ which is comparable to $\tau_m = 1/\Omega_m$, the system will enter a stationary state under the adiabatic elimination satisfying $\dot{\tilde{\alpha}}_{j0} = \dot{\tilde{\alpha}}_j = 0$. By substituting $\dot{\tilde{\alpha}}_{j0} = \dot{\tilde{\alpha}}_j = 0$ into Eq. (S.14) and omitting higher-order harmonic terms, it can be solved that $\tilde{\beta}_{j0} \approx 0$ and

$$\tilde{\alpha}_j = \frac{ig_{om}\left(\tilde{\beta}_j - \tilde{\beta}_{j+1}\right)}{\left[\gamma + i\left(\Delta - \Omega_m\right)\right]}\tilde{\alpha}_{j0} + \frac{i\sqrt{2\gamma_{\text{ext}}}}{\left[\gamma + i\left(\Delta - \Omega_m\right)\right]}\tilde{\varepsilon}, \tag{S.17}$$

$$\tilde{\alpha}_{j0} \approx -\frac{g_{om}\sqrt{2\gamma_{\text{ext}}}\tilde{\varepsilon}}{\left(\gamma + i\Delta\right)\left[\gamma + i\left(\Delta - \Omega_m\right)\right]}\left(\tilde{\beta}_j - \tilde{\beta}_{j+1}\right) + \frac{i\sqrt{2\gamma_{\text{ext}}}}{\left(\gamma + i\Delta\right)}\varepsilon. \tag{S.18}$$

By substituting Eqs. (S.17) and (S.18) into Eq. (S.15) and omitting higher-order nonlinear terms, we have

$$\begin{aligned}\dot{\tilde{\beta}}_j(t) \approx & \frac{2\gamma_{\text{ext}}\gamma g_{om}^2\left|\varepsilon\right|^2}{\left[\gamma^2 + \left(\Delta - \Omega_m\right)^2\right]\left(\gamma^2 + \Delta^2\right)}\left(\tilde{\beta}_{j-1} - \tilde{\beta}_{j+1}\right) \\ & + \frac{8\gamma_{\text{ext}} g_{om}^5 \gamma^2 \gamma_{\text{ext}} \Delta\left|\varepsilon\right|^4}{\left[\gamma^2 + \left(\Delta - \Omega_m\right)^2\right]^2\left(\gamma^2 + \Delta^2\right)^3 \Gamma_m}\left\{\left(\tilde{\beta}_{j-1} - \tilde{\beta}_j\right)^2 - \left(\tilde{\beta}_j - \tilde{\beta}_{j+1}\right)^2\right\}.\end{aligned} \tag{S.19}$$

Let k be the wave vector of the collective mechanical mode, then we have

$$\tilde{\beta}_j = A\exp\left[i\left(kjR\right)\right], \tag{S.20}$$

where A is the amplitude of the mechanical traveling wave, and R is the radius of the microtoroid. We then take the continuous limit by letting $z = jR$, $u = A\exp\left(ikz\right)$ and taking $R \to 0$, then we have

$$\begin{aligned}\tilde{\beta}_{j\pm1} = Ae^{ikjR}e^{\pm ikR} &\approx Ae^{i\,kjR}\left(1 \pm ikR - \frac{1}{2}k^2R^2 \mp \frac{i}{6}k^3R^3 + \frac{1}{24}k^4R^4\right) \\ &= u \pm R\frac{\partial u}{\partial z} + \frac{R^2}{2}\frac{\partial^2 u}{\partial z^2} \pm \frac{R^3}{6}\frac{\partial^3 u}{\partial z^3} + \frac{R^4}{24}\frac{\partial^4 u}{\partial z^4}.\end{aligned} \tag{S.21}$$

Thus, it can be shown from Eq. (S.21) that

$$\tilde{\beta}_{j-1}-\tilde{\beta}_{j+1}\approx -2R\frac{\partial u}{\partial z}-\frac{R^3}{3}\frac{\partial^3 u}{\partial z^3}, \tag{S.22}$$

$$\left(\tilde{\beta}_{j-1}-\tilde{\beta}_{j}\right)^2-\left(\tilde{\beta}_{j}-\tilde{\beta}_{j+1}\right)^2\approx -2k^2R^3u\frac{\partial u}{\partial z}. \tag{S.23}$$

By substituting Eqs. (S.22) and (S.23) into Eq. (S.19) and noting that the input pump power P_{pump} is linearly proportional to the square of the amplitude of the input field ε, i.e., $|\varepsilon|^2=\alpha_1 P_{\text{pump}}$, where α_1 is a proportional constant, we have

$$\frac{\partial u}{\partial t}=\left[\left(G-\Gamma_m\right)-\xi u^2\right]u-v\frac{\partial u}{\partial z}-\sigma\, u\frac{\partial u}{\partial z}-d_{\text{kdV}}\frac{\partial^3 u}{\partial z^3}, \tag{S.24}$$

where

$$v=\frac{4\gamma_{\text{ext}}g_{om}^2\alpha_1 P_{\text{pump}}\gamma R}{\left[\gamma^2+\left(\Delta-\Omega_m\right)^2\right]\left(\gamma^2+\Delta^2\right)}, \tag{S.25}$$

$$d_{\text{kdV}}=\frac{2\gamma_{\text{ext}}g_{om}^2\alpha_1 P_{\text{pump}}\gamma R^3}{3\left[\gamma^2+\left(\Delta-\Omega_m\right)^2\right]\left(\gamma^2+\Delta^2\right)}, \tag{S.26}$$

$$\sigma=\frac{8\gamma_{\text{ext}}^2g_{om}^5\gamma^2k^2\alpha_1^2P_{\text{pump}}^2\Delta R^3}{\left[\gamma^2+\left(\Delta-\Omega_m\right)^2\right]^2\left(\gamma^2+\Delta^2\right)^3\Gamma_m}. \tag{S.27}$$

If we further consider the noise term such as thermal noise acting on the mechanical mode, we can obtain the dynamical equation of the mechanical mode

$$\frac{\partial u}{\partial t}=\left[\left(G-\Gamma_m\right)-\xi u^2\right]u-v\frac{\partial u}{\partial z}-\sigma\, u\frac{\partial u}{\partial z}-d_{\text{kdV}}\frac{\partial^3 u}{\partial z^3}+\zeta(t), \tag{S.28}$$

where $\zeta(t)$ is assumed to be white noise satisfying

$$E\left(\zeta\left(t\right)\right)=0,\ E\left(\zeta\left(t\right)\zeta\left(t'\right)\right)=D\delta\left(t-t'\right), \tag{S.29}$$

and the strength of the noise D is assumed to be far-smaller than other parameters. Note that Eq. (S.28) is a modified Korteweg–de Vries equation with additional mechanical loss, gain, nonlinear saturation terms and noise term and the Korteweg–de Vries equation [S5, S6, S7] can be used to represent a uni-directional propagation of weakly-nonlinear long wave like a shallow-water wave with a weakly-nonlinear restoring force, where long wave means that the wavelength of the wave is much larger than the thickness of the medium. Here z is the coordinate in the radial direction of the microtoroid; u is the envelop of the mechanical motion; v is the propagation velocity of the mechanical traveling wave; σ is the nonlinear coefficient of mechanical motion; and d_{kdV} is the optomechanics-induced dispersion rate of phonon propagation. When $G>\Gamma_m$, the stochastic noise $\xi\left(t\right)$ will drive the system away from the equilibrium point, and a dissipative structure appears when the amplitude of the stationary state is large enough such that the mechanical gain is well balanced by the mechanical loss and the saturation effects. Depending on the system parameters, this dissipative structure can be periodic oscillation (limit cycle), periodic pulses (cnoidal-wave solution), or single pulse (soliton solution). In fact, when the energy fed into the mechanical system by optomechanics is small, this dissipative structure supports a stable periodic motion called limit cycle, which is similar to self-sustaining oscillations in the van der Pol equation. Here we change the system parameters such as the frequency detuning between the optical cavity mode and the input field, which can be seen as the order parameters in the dissipative structure theory. When we change these bifurcation parameters, the system will change from one type of dissipative structures such as the periodic motion to another type of dissipative structures such as

the cnoidal-wave solution or the soliton solution. This phase transition is also known as dynamical bifurcation [S8] .

From Eq. (S.28), the dispersion relation of the propagating mechanical traveling wave is given by

$$\omega_\mu = \Omega_m + vk + d_{\mathrm{kdV}}k^3 = \Omega_m + D_1\mu + D_3\mu^3, \tag{S.30}$$

where $\mu = (\lambda k)/(2\pi)$ is the relative mode number, and λ is the wavelength of the fundamental vibrational mode. The dispersion curves of the mechanical traveling wave for different detuning frequencies and different pump powers are given in Fig. S2a and Fig. S2b.

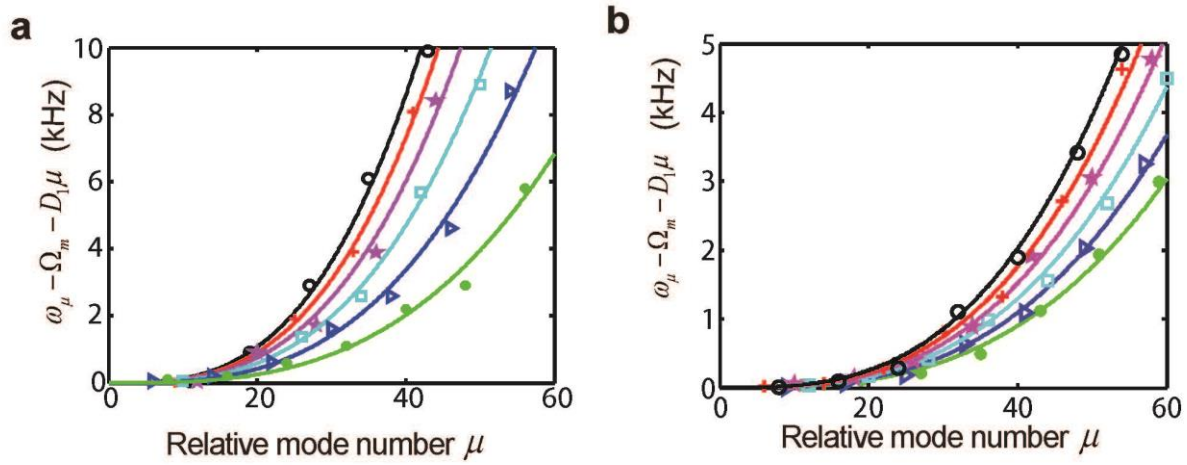

Figure S2. Dispersion curves for the mechanical mode. a, The mode dispersion spectra for different detuning frequencies. The normalized detuning frequencies for the curves from up to down are 0.871, 0.865, 0.858, 0.852, 0.845, and 0.839. **b,** The mode dispersion spectra for different pump powers. The pump powers for the curves from up to down are 26.01mW, 22.65 mW, 19.53 mW, 16.64 mW, 13.98 mW, and 11.56 mW.

The modified Korteweg–de Vries equation (S.28) has various stationary solutions in different parameter regimes. Given parameters $\Omega_m = 27.3\,\text{MHz}$, $\Gamma_m = 40\,\text{kHz}$, $R = 30\ \mu\text{m}$, $g_{om} = 1.5\,\text{kHz}$, $\Delta = 27\ \text{MHz}$, $\gamma = 12\ \text{MHz}$, $\gamma_{\text{ext}} = 6\,\text{MHz}$, and $\alpha_1 = 3.99\times10^6\ \text{MHz/mW}$, we plot the time-domain and frequency-domain signals of the sinusoidal periodic solution in Fig. S3a and S3b, the time-domain and frequency-domain signals of the cnoidal-wave solution (periodic pulses) in Fig. S3c and S3d, and the time-domain and frequency-domain signals of the soliton solution (single pulse) in Fig. S3e and S3f, which fits very well with what we observe in experiments.

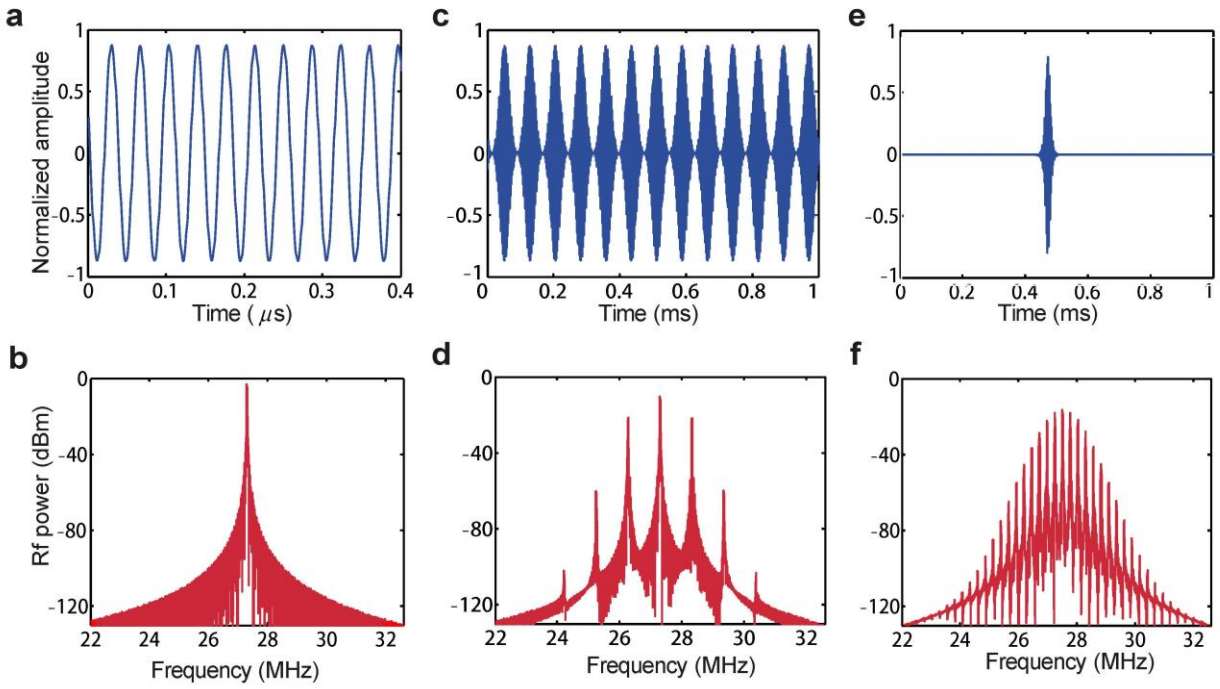

Figure S3. Numerical simulation results in different regimes for the mechanical mode. a, c, e, Time domain signals of the periodic solution (left) with $P_{pump} = 14.9\ \text{mW}$, cnoidal-wave solution (middle) with $P_{pump} = 17.2\ \text{mW}$, and soliton solution (right) with $P_{pump} = 18.8\ \text{mW}$. The input power increases from left to right and we can see the localization of phonon with increasing pump

power. **b, d, f,** Output spectra of the pump field in periodic (left, single peak), cnoidal wave (middle, frequency-comb-type spectrum), and soliton (right, broad-band peak) regimes.

II. CNOIDAL-WAVE SOLUTION OF THE MECHANICAL TRAVELLING-WAVE EQUATION

The modified Korteweg-de Vries equation (S.28) supports stationary periodic solutions, called the cnoidal-wave solutions [S7] . Given the parameters $\Omega_m = 27.3\,\mathrm{MHz}$, $\Gamma_m = 40\,\mathrm{kHz}$, $R = 30\ \mu\mathrm{m}$, $g_{om} = 1.5\ k\mathrm{Hz}$, $\gamma = 12\ \mathrm{MHz}$, $\gamma_{\mathrm{ext}} = 6\ \mathrm{MHz}$, and $\alpha_1 = 3.99\times10^{6}\ \mathrm{MHz/mW}$, we plot the width of the pulse versus the normalized detuning frequency $\delta = \Delta/\Omega_m$ and the pump power in Figs. S4a and S4d, respectively. The period of the pulse versus the normalized detuning frequency $\delta = \Delta/\Omega_m$ and the pump power are presented in Figs. S4b and S4e, respectively. The amplitude of the pulse versus the normalized detuning frequency $\delta = \Delta/\Omega_m$ and the pump power are denoted in Figs. S4c and S4f, respectively. The trends of the curves fit very well with what we observe in experiments.

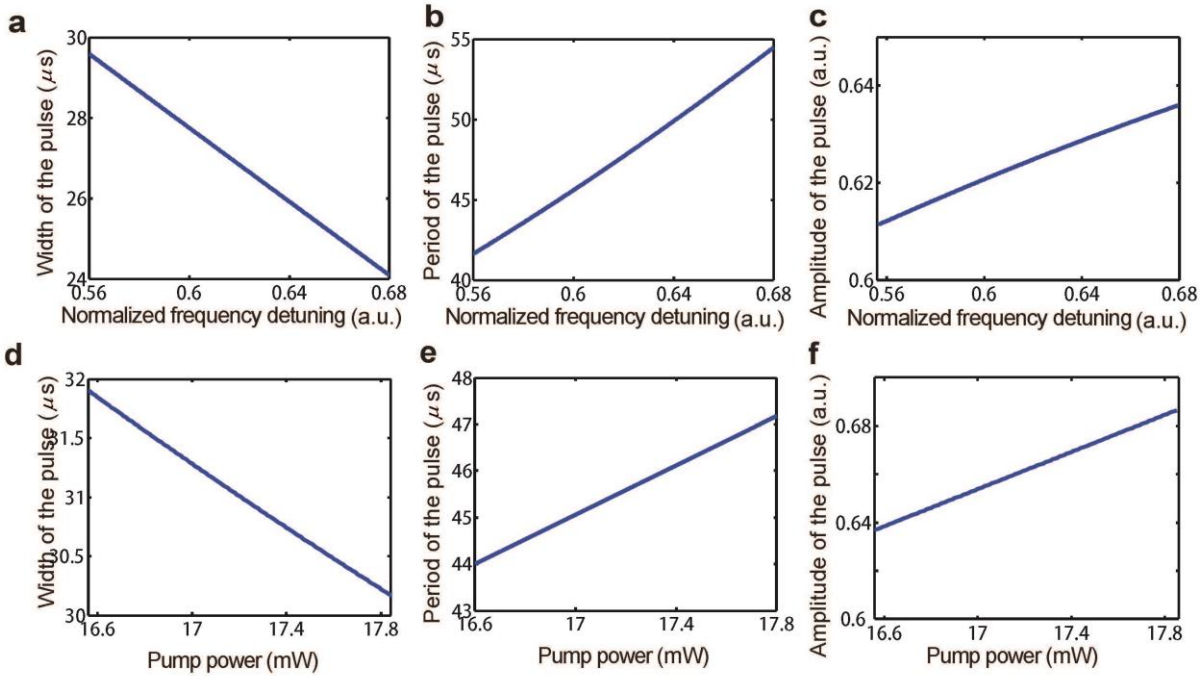

Figure S4. Numerical results for different parameters of the localized phononic wavepacket in the cnoidal-wave regime. a-c, Widths, periods, and amplitudes of the localized phononic wavepackets versus different detuing frequencies of the input field. **d-f,** Widths, periods, and amplitudes of the localized phononic wavepackets versus different pump powers. It is shown that the widths of the localized phonon wavepackets will decrease and the periods and amplitudes of the pulses will increase when we increase the detuing frequency or the input pump power.

III. MULTI-SOLITON SOLUTION OF THE MECHANICAL TRAVELLING-WAVE EQUATION

Between the cnoidal-wave regime and the single-soliton regime, there exists a narrow unstable regime in which multi pulses can be observed, but the time intervals between different pulses are not fixed like the cnoidal wave regime. We call it the multi-soliton regime. We plot in Fig. S5 the

multi-soliton pulses. With the increase of the detuning frequency of the input field, we see the transition from the eight-soliton pulses in Fig. S5a to the single-soliton pulses in Fig. S5h.

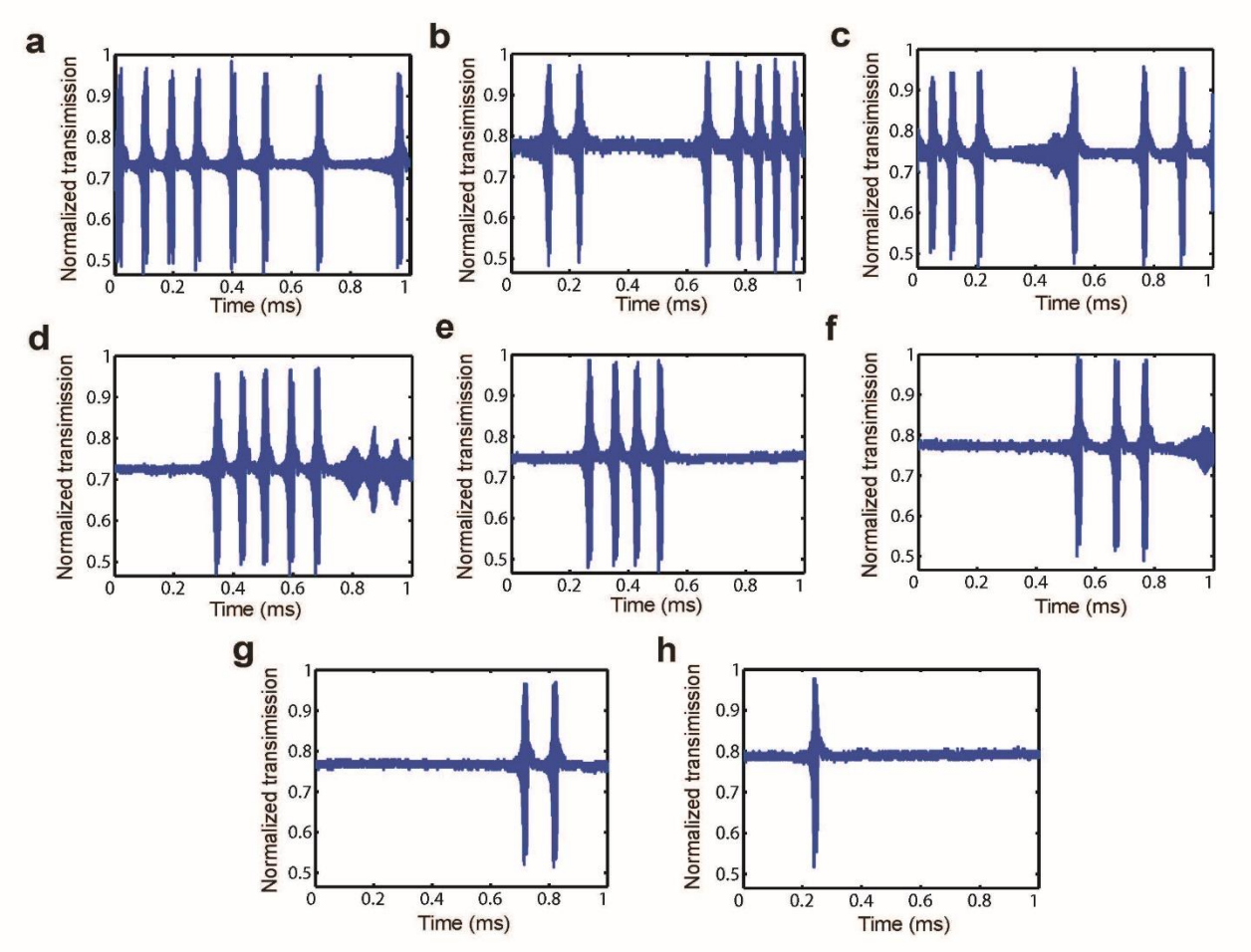

Figure S5. Experimental data for multi-soliton wavepackets. From **a** to **h**, with increased detuning frequency, eight-soliton pulse to a single-soliton pulse are presented.

Although the multi-soliton regime results from nonlinearity in Eq. (S.28), we are able to analyze the maximum allowable number of solitons in the regime. To further understand how many solitary waves exist in the multi-solitary regime, we first investigate the interaction of two solitons propagating in the same direction. Under the condition that $G-\Gamma_m, \xi, D \ll v, \sigma, d_{\mathrm{kdV}}$, we can omit the effects of gain, loss, and nonlinear saturation terms and noise terms in the stationary state, and

then we employ the split-step method to solve the stationary KdV-like equation by evolving the unit-time step, as illustrated in Fig. S6. We can split the KdV equation to its linear

$$\frac{\partial u}{\partial t} = -v\frac{\partial u}{\partial z} - d_{\mathrm{kdV}}\frac{\partial^3 u}{\partial z^3}, \tag{S.31}$$

and nonlinear parts

$$\frac{\partial u}{\partial t} = -\sigma\, u\frac{\partial u}{\partial z}. \tag{S.32}$$

Taking the Fourier transform in k space, they become

$$\tilde{u}(k,t) = \tilde{u}(k,0)\mathrm{e}^{\left(-ikv+ik^3 d_{KdV}\right)t}, \tag{S.33}$$

and

$$\tilde{u}_t(k,t) = -\frac{k\sigma}{2}u^2. \tag{S.34}$$

Now we calculate them using the finite difference method like the Euler or Runge-Kutta methods. For instance, with the Euler method we simply derive them as

$$\tilde{u}_1\left(k,t+\Delta t\right) = \tilde{u}\left(k,t\right)e^{\left(-ikv+ik^3 d_{\mathrm{KdV}}\right)\Delta t}, \tag{S.35}$$

$$\tilde{u}\left(k,t+\Delta t\right) = \tilde{u}_1\left(k,t+\Delta t\right) - \frac{k\sigma}{2}\Delta t\left|u_1\right|^2\left(k,t+\Delta t\right) = \tilde{u}_1\left(k,t+\Delta t\right) - \frac{k\sigma}{2}\Delta t\, F\left(\left\{F^{-1}\left[\tilde{u}_1\left(k,t+\Delta t\right)\right]\right\}^2\right). \tag{S.36}$$

where $F(\ldots)$ and $F(\ldots)^{-1}$ is the Fourier transform and inverse Fourier transform, respectively, and they are all calculated by the FFT algorithm. Here Δt is the unit time step, at the heart of the split-step method. Once we evaluate $\tilde{u}(k,t)$ over the time range of interest, $u(z, t)$ is finally obtained via the inverse FFT.

Considering the solution of two solitons in the KdV equation, the amplitude ratio of the solitons is given by

$$\varepsilon = \frac{\sqrt{\eta_2} - \sqrt{\eta_1}}{\sqrt{\eta_2} + \sqrt{\eta_1}}, \tag{S.37}$$

where η_1 and η_2 are the amplitudes of two solitons. It was well known that the solution of two solitons in the KdV equation can pass through each other when the two solitons have distinct amplitudes (See Fig S6.c and d). In a case of having similar amplitudes, that is, $\varepsilon < 0.236$, however two solitons do not collide but bounce off, thereby showing avoided crossing as illustrated in Fig. S6a and b [S9, S10]. It was shown in [S10] that the minimum separation distance is around $2\log(2/0.236) = 4.27$ for the normalized KdV equation. After scaling up, the minimum separation distance in our systems is thus given by $\Delta\Phi = 4.27\sqrt{3d_{KdV}/\sigma}$. Similarly, we can derive the minimum separation time by dividing it to the soliton velocity v_1. Given the parameters $\Omega_m = 27.3\,\text{MHz}$, $\Gamma_m = 40\,k\text{Hz}$, $R = 30\,\mu\text{m}$, $g_{om} = 1.5\,k\text{Hz}$, $\gamma = 12\,\text{MHz}$, $\gamma_{\text{ext}} = 6\,\text{MHz}$, $\alpha_1 = 3.99\times10^6\ \text{MHz/mW}$, $P_{pump} = 16\,\text{mW}$ and $\delta = \Delta/\Omega_m = 0.7$, the minimum separation time is calculated for the multi-soliton regime $\tau_{\min} = \frac{\Delta\Phi}{v_1} = 36\,\mu\text{sec}$, which is notably close to the measured distance in Fig S5. Under the condition, a possible limit of a maximum number of solitons in the multi-soliton regime is estimated $N_{\max} = 28$ within 1 millisecond spanning. We confirm that the eight-soliton pulse in 1 millisecond that is smaller than the estimated maximum number of solitons $N_{\max}$ as shown in Fig. S5a.

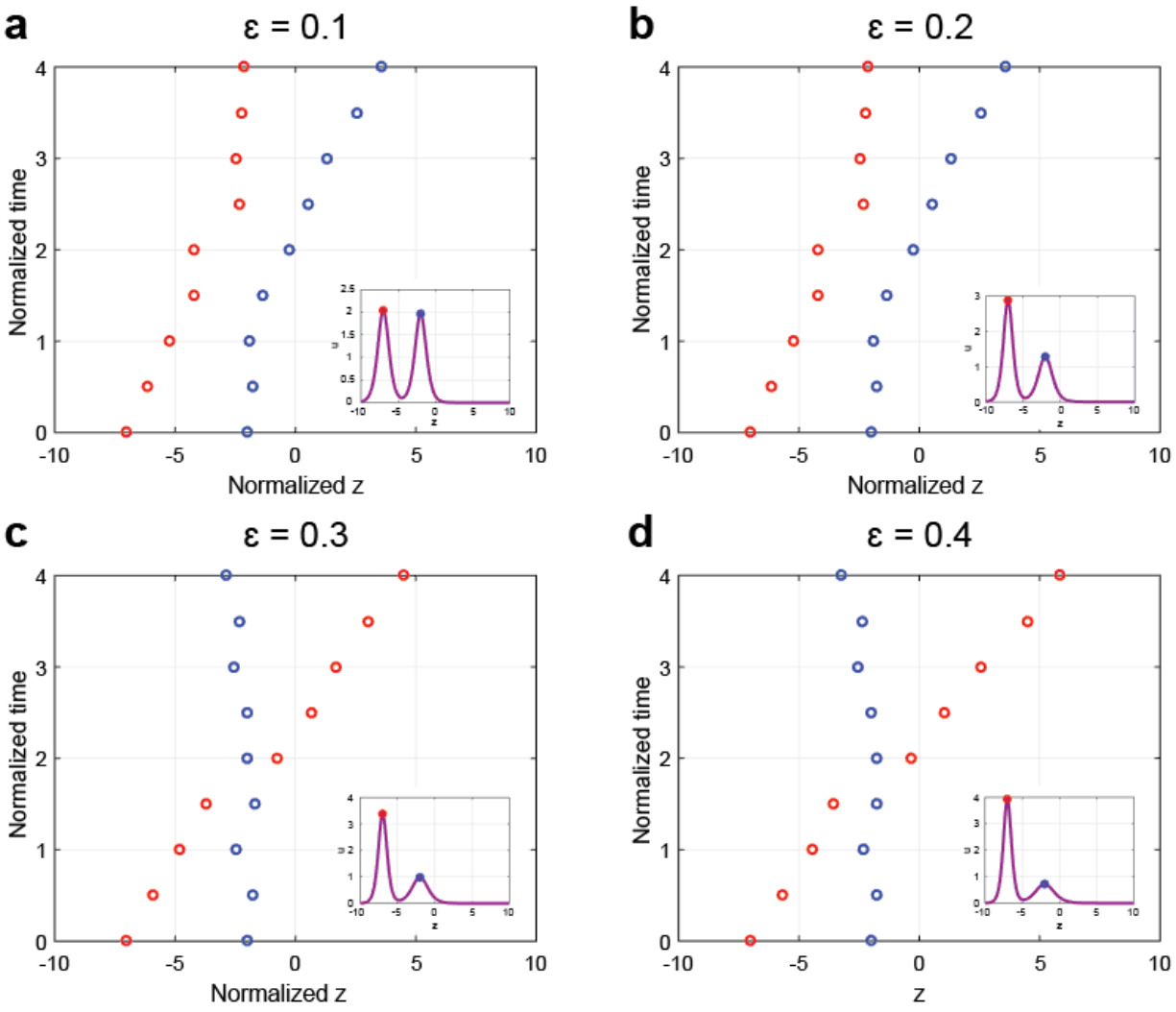

Figure S6. Interactions of two solitons having different ε from 0.1 to 0.4. We numerically simulate the interaction of two solitons which initially propagate in the same direction. Here the red (and blue) dots represent the peaks of the left (and right) solitary waves. The insets (purple) show initial positions of two solitons located at $z=-7$ and $z=-2$, respectively. **a-b,** For $\varepsilon<0.236$, two solitons propagate in the same direction and interact with one other. Here we observe avoid crossing of two solitons. **c-d**. For $\varepsilon>0.236$, two solitons collide and pass through each other. Due to exchanging energy, the smaller soliton (blue dots) slightly travels in the opposite direction.

IV. SINGLE-SOLITON SOLUTION OF THE MECHANICAL TRAVELLING-WAVE EQUATION

The modified Korteweg-de Vries equation (S.28) also supports single-soliton solution. Given the parameters $\Omega_m = 27.3\,\mathrm{MHz}$, $\Gamma_m = 40\,k\mathrm{Hz}$, $R = 30\,\mu\mathrm{m}$, $g_{om} = 1.5\,k\mathrm{Hz}$, $\gamma = 12\ \mathrm{MHz}$, $\gamma_{\mathrm{ext}} = 6\ \mathrm{MHz}$, and $\alpha_1 = 3.99\times10^{6}\ \mathrm{MHz/mW}$, we show in Fig. S6a-S6c the phononic wavepacket localization process for a fixed detuning frequency $\delta = \Delta/\Omega_m = 0.87$ and increasing input pump powers of $16\,\mathrm{mW}$, $25\,\mathrm{mW}$, and $28\,\mathrm{mW}$. The width of the pulse versus the normalized detuning frequency $\delta = \Delta/\Omega_m$ and the pump power are presented in Fig. S6d and Fig. S6f, respectively. The amplitude of the pulse versus the normalized detuning frequency $\delta = \Delta/\Omega_m$ and the pump power are denoted in Fig. S6e and Fig. S6g, respectively. The simulation results fit very well with what we observe in experiments.

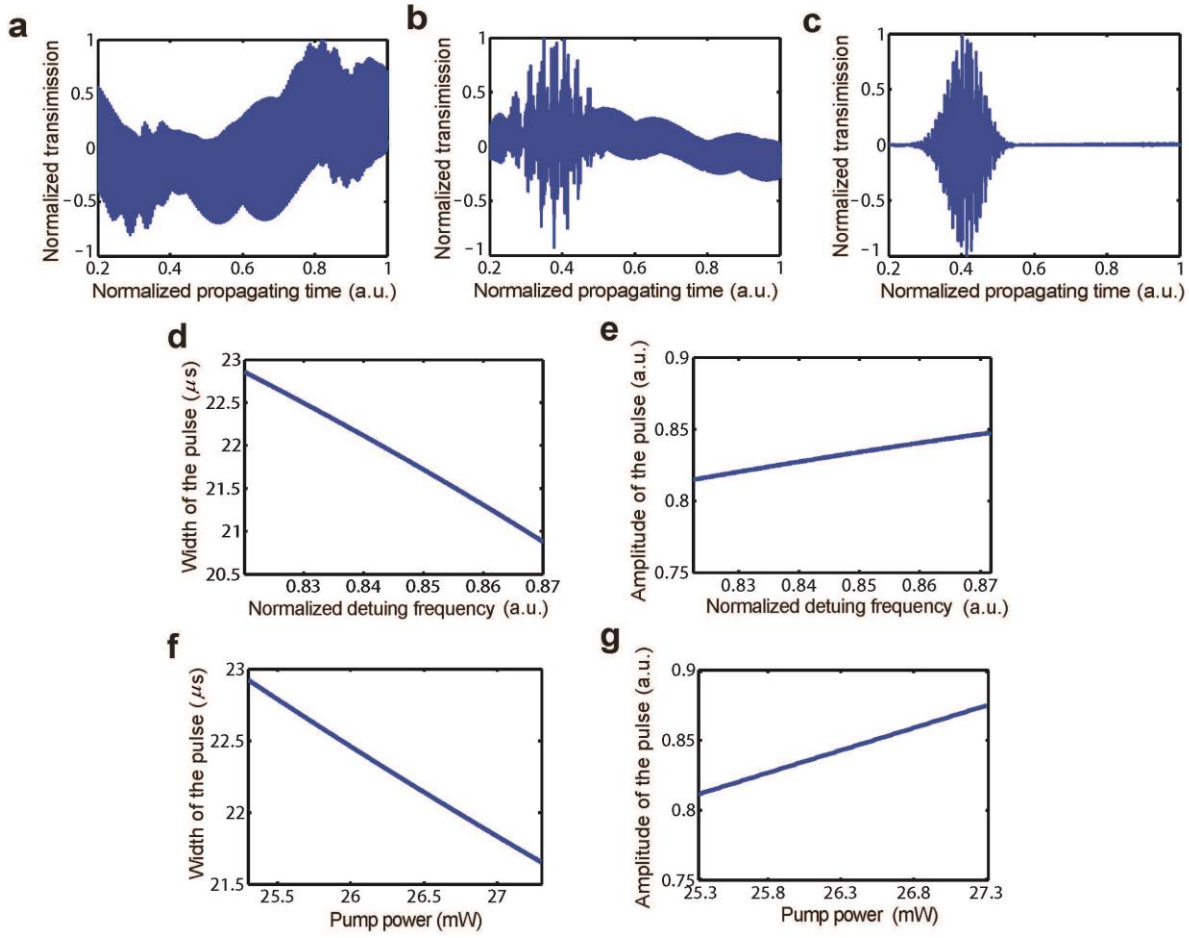

Figure S7. Numerical results for phononic wavepacket localization in the single-soliton regime. a-c, Phononic wavepacket localization with a fixed detuning frequency $\delta = \Delta/\Omega_m = 0.87$ and increasing input pump power of 16 mW, 25 mW, and 28 mW. **d, e,** Widths and amplitudes of the localized phonon wavepackets versus different detuing frequencies of the input field. **f, g,** Widths and amplitudes of the localized phonon wavepackets versus different pump power. It is shown that the widths of the localized phonon wavepackets will decrease and the amplitudes of the pulses will increase when we increase the detuing frequency or the input pump power.

V. OPTOMECHANICALLY-INDUCED OPTICAL SOLITON

Similar frequency-comb-type spectra as shown in Fig. 2f have been reported in other optomechanical systems, such as in dual-nanoweb optomechanical fibres. In these geometries, the frequency-comb has been attributed to a cascaded optical four-wave mixing process induced by optomechanical nonlinearity. In contrast, the localized wave-packets observed in our experiments are induced by the localized mechanical motion of the microtoroid, rather than optomechanical-nonlinearity-induced localized photonic wave-packet (optical solitons). We present the time-domain signal of the optical soliton induced by optomechanics (see also our analysis in section V in the supplement) in Fig. 3m and its corresponding frequency spectrum in Fig. 3n. By comparing Fig. 2d and Fig. 3m, it is shown that the width of the optical soliton pulses induced by optomechanics is at least six orders of magnitude smaller than the one of the pulses observed in our experiments confirming the inherent mechanical nature of the observed solitons.

There is another possible way to explain the localized wavepacket observed in the output field in our experiments in which the localized wavepacket is induced by the localized optical field, i.e., optical soliton which is generated by the optomechanical nonlinearity and dispersion of the optical field in silica. However, we find that such kind of explanation cannot fit with our experimental data and thus is not what we observed in experiments. To show this, let us first begin with the Hamiltonian of the optomechanical system

$$H = \Delta\alpha^{\dagger}\alpha + \sqrt{\kappa_{\text{ext}}}\varepsilon\left(\alpha^{\dagger} + \alpha\right) + g_{om}\alpha^{\dagger}\alpha\ X + \frac{\Omega_m}{2}\left(X^2 + P^2\right), \tag{S.38}$$

where the first and second terms are related to the free evolution of the optical field α, and the third term explains the interaction between the optical field and the mechanical mode with X and P representing the position and momentum of the mechanical oscillator, respectively. The last

term corresponds to the free evolution of the mechanical mode. By introducing the translational transformation

$$\widehat{X} = X + \frac{g_{om}}{\Omega_m}\alpha^{\dagger}\alpha, \quad \widehat{P} = P, \tag{S.39}$$

the Hamiltonian H can be re-expressed as

$$H = \Delta\alpha^{\dagger}\alpha + \sqrt{\kappa_{\text{ext}}}\varepsilon\left(\alpha^{\dagger} + \alpha\right) - \frac{g_{om}^2}{2\Omega_m}\left(\alpha^{\dagger}\alpha\right)^2 + \frac{\Omega_m}{2}\left(\widehat{X}^2 + \widehat{P}^2\right), \tag{S.40}$$

where we see that the nonlinear interaction between the optical field and the mechanical motion leads to an effective Kerr-type nonlinearity in the optical mode α, with Kerr coefficient given as

$$\mu_{\text{kerr}} = \frac{g_{om}^2}{2\Omega_m}, \tag{S.41}$$

where Ω_m is the frequency of the mechanical mode. Equation (S.41) implies that the optomechanically-induced Kerr-type nonlinearity is dependent on (i) the optomechanical coupling between the optical and mechanical modes and (ii) the frequency of the mechanical mode. If we further consider the dispersion effects of the optical field in silica, the optomechanics-induced nonlinear dispersive wavepacket-propagating equation of the optical mode can be represented by

$$\frac{\partial\alpha}{\partial t} + \frac{c}{R}\frac{\partial\alpha}{\partial\theta} - \left(\gamma + i\Delta\right)\alpha = -id_{\text{NSE}}\frac{\partial^2\alpha}{\partial\theta^2} - i\mu_{\text{Kerr}}\left|\alpha\right|^2\alpha + \sqrt{2\gamma_{\text{ext}}}\varepsilon, \tag{S.42}$$

where θ is the polar angle coordinate inside the resonator, and c and d_{NSE} are the speed of light and the dispersion rate of photon propagating inside silica, respectively. This equation is a modified version of the so-called nonlinear Schrodinger equation which supports solition-type solution that can be represented by

$$\alpha(t)=\left(\frac{2\gamma_{\text{ext}}\varepsilon^2}{\mu_{\text{kerr}}}\right)^{1/6}+\eta_0 e^{-(\gamma+i\Delta)t-i\phi}\,\text{sech}\left[\left(\frac{\eta_0^2\mu_{\text{kerr}}}{2d_{\text{NSE}}}\right)^{1/2}\left(\theta-\frac{c}{R}t\right)\right]. \tag{S.43}$$

It can be shown that the soliton pulses observed in our experiments and the optical soliton pulses given by Eq. (S.43) are in quite different regimes. To show this, given the system parameters $\Omega_m = 27.3\,\text{MHz}$, $\Gamma_m = 0.4\,\text{MHz}$, $R = 30\,\mu\text{m}$, $g_{om} = 3\,k\text{Hz}$, $\Delta = 27\,\text{MHz}$, $\gamma = 12\,\text{MHz}$, $\gamma_{\text{ext}} = 6\,\text{MHz}$, and $d_{\text{NSE}} = 1\,k\text{Hz}$, we present the time-domain signal of the optical soliton given by Eq. (S.51) in Fig.S8a and its corresponding spectrum in Fig.S8b. By comparing Fig.S3 and Fig.S8, we can see that the mechanical soliton pulses and the optical soliton pulses are in quite different regimes (the width of the mechanical-soliton time-domain pulses are six-order of magnitude smaller than that of optical soliton), and what we observe in experiments fits well with those by mechanical soliton. To further confirm if the localized microwave pulses are induced by localized optical domain signals, we check the spectra of the output optical signals by optical spectrum analyzer, and we do not see any evidence for localized photon effects when the microtoroid resonator is in the mechanical cnoidal-wave regime and the soliton regime (see Fig. S8c and Fig. S8d). Thus what we observe in experiments fits well with those by mechanical soliton rather than optical soliton.

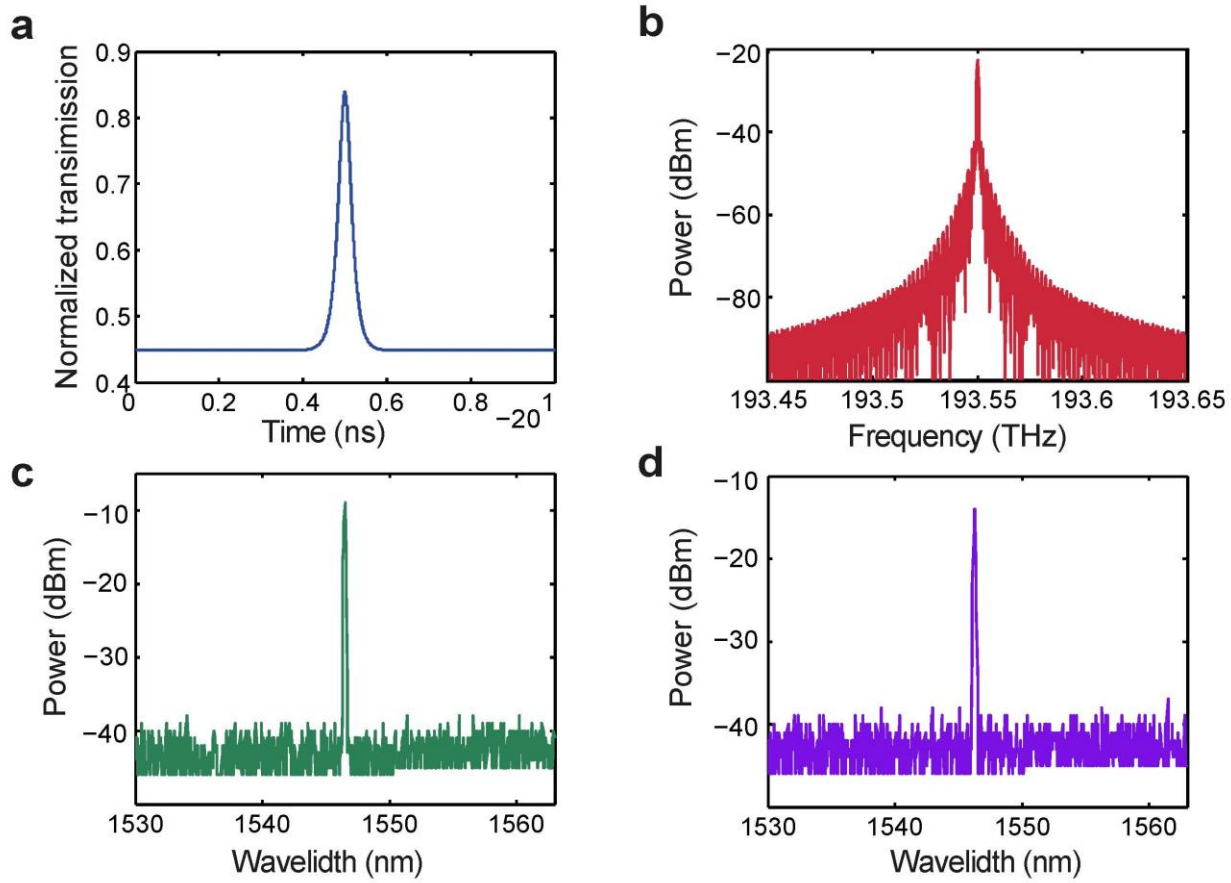

Figure S8. Numerical simulation and experimental results for optical soliton induced by optomechanical nonlinearity. a, Time domain signals of the optomechanics-induced optical soliton given by Eq. (S.43). **b,** Spectrum of the optomechanics-induced optical soliton. The width of the optical soliton is in the regime of ns, which is six-order of magnitude smaller than those pulses induced by mechanical soliton. The width of the spectrum of the optical soliton is in the regime of THz which is six-order of magnitude larger than those pluses generated by mechanical soliton. **c,** Optical spectrum read by optical spectrum analyzer when the microtoroid resonator is in the soliton regime. **d,** Optical spectrum read by optical spectrum analyzer when the microtoroid resonator is in the cnoidal-wave regime.

VI. SENSING BY OPTOMECHANICAL SOLITONS

In this section, we study the sensing application of the optomechanical soliton and consider the detection of the vibration of a cantilever tip as an example. The dynamical equation of the optical mode of the microtoroid can be expressed as

$$\dot{\alpha} = -\left(\gamma + i\Delta\right)\alpha + ig_{om}x_{\beta}\left(t\right)\alpha + ig_{x}x_{\mathrm{tip}}\left(t\right)\alpha + i\sqrt{\gamma_{\mathrm{ext}}}\varepsilon_{d}, \tag{S.44}$$

where $\alpha\left(t\right)$ is the amplitude of the optical mode of the microtoroid. $x_{\beta}\left(t\right)$ is the normalized position of the mechanical mode of the microtoroid. $x_{\mathrm{tip}}\left(t\right)$ is the position of the cantilever tip needed to be measured and g_{x} is the coupling strength between the optomechanical resonator and the cantilever tip. Let us assume that

$$x_{\mathrm{tip}}\left(t\right) = -A_{\mathrm{tip}}\cos\left(\omega_{\mathrm{tip}}t + \phi_{\mathrm{tip}}\right), \tag{S.45}$$

$$x_{\beta}\left(t\right) = -\sum_{\delta} A_{\delta}\cos\left(\omega_{\delta}t + \phi_{\delta}\right), \tag{S.46}$$

where $A_{\mathrm{tip}}, \omega_{\mathrm{tip}}, \phi_{\mathrm{tip}}$ are the amplitude, the eigenfrequency, and the initial phase of the cantilever tip. $A_{\delta}, \omega_{\delta}, \phi_{\delta}$ are the amplitude, the eigenfrequency, and the initial phase of the δ-th mechanical sub-mode of the optomechanical resonator. The analytical solution of Eq. (S.64) can be written as

$$\alpha\left(t\right) = \int_{0}^{t} Q\left(\tau\right)e^{-\int_{\tau}^{t}P(\theta)d\theta}d\tau, \tag{S.47}$$

where

$$\begin{aligned} P\left(t\right) &= \gamma + i\Delta - ig_{om}x_{\beta}\left(t\right) - ig_{x}x_{\mathrm{tip}}\left(t\right) \\ &= \gamma + i\Delta + ig_{om}\sum_{\delta} A_{\delta}\cos\left(\omega_{\delta}t + \phi_{\delta}\right) + ig_{x}A_{\mathrm{tip}}\cos\left(\omega_{\mathrm{tip}}t + \phi_{\mathrm{tip}}\right), \end{aligned} \tag{S.48}$$

$$Q\left(t\right) = i\sqrt{\gamma_{\mathrm{ext}}}\varepsilon_{d}. \tag{S.49}$$

To simplify Eq. (S.47) further, we use the following equation

$$e^{ix\sin y} = \sum_{n} J_{n}\left(x\right)e^{iny}, \tag{S.50}$$

where $J_n(x)$ are the n-order Bessel functions which can be expanded as

$$\begin{aligned} J_0(x) &= 1-\frac{1}{4}x^2+\frac{1}{64}x^4+\cdots, \\ J_1(x) &= \frac{1}{2}x-\frac{1}{16}x^3+\cdots \end{aligned} \tag{S.51}$$

Thus, we have

$$\begin{aligned} e^{\int_\tau^t P(\theta)d\theta} &= e^{(\gamma+i\Delta)(t-\tau)}e^{\frac{ig_xA_{\text{tip}}}{\omega_{\text{tip}}}\left[\sin(\omega_{\text{tip}}t+\phi_{\text{tip}})-\sin(\omega_{\text{tip}}\tau+\phi_{\text{tip}})\right]}\prod_\delta e^{\frac{ig_{om}A_\delta}{\omega_\delta}\left[\sin(\omega_\delta t+\phi_\delta)-\sin(\omega_\delta\tau+\phi_\delta)\right]} \\ &\approx e^{(\gamma+i\Delta)(t-\tau)}e^{\frac{ig_xA_{\text{tip}}}{\omega_{\text{tip}}}\left[\sin(\omega_{\text{tip}}t+\phi_{\text{tip}})-\sin(\omega_{\text{tip}}\tau+\phi_{\text{tip}})\right]}\prod_\delta J_0\left(\frac{g_{om}A_\delta}{\omega_\delta}\right)J_0\left(-\frac{g_{om}A_\delta}{\omega_\delta}\right) \\ &= e^{(\gamma+i\Delta)(t-\tau)}e^{\frac{ig_xA_{\text{tip}}}{\omega_{\text{tip}}}\left[\sin(\omega_{\text{tip}}t+\phi_{\text{tip}})-\sin(\omega_{\text{tip}}\tau+\phi_{\text{tip}})\right]}\prod_\delta J_0^2\left(\frac{g_{om}A_\delta}{\omega_\delta}\right). \end{aligned} \tag{S.52}$$

Note that

$$\begin{aligned} \prod_\delta J_0\left(\frac{g_{om}A_\delta}{\omega_\delta}\right) &= \exp\left[\sum_\delta \log J_0\left(\frac{g_{om}A_\delta}{\omega_\delta}\right)\right] \approx \exp\left(-\frac{g_{om}^2}{4}\sum_\delta\frac{A_\delta^2}{\omega_\delta^2}\right) \\ &= \exp\left[-\frac{\pi g_{om}^2}{2}\int_{\omega_{c1}}^{\omega_{c2}}\frac{S_\beta(\omega)}{\omega^2}d\omega\right] \triangleq \eta_{\text{enh}}^{-1/2}, \end{aligned} \tag{S.53}$$

where ω_{c1} and ω_{c2} are the lower and higher bounds of the mechanical frequencies of the sub-modes contribute to the response of the vibration of the cantilever tip. By substituting Eq. (S.53) into Eq. (S.52), we have

$$e^{\int_\tau^t P(\theta)d\theta} = \eta_{\text{enh}}^{-1}e^{(\gamma+i\Delta)(t-\tau)}e^{\frac{ig_xA_{\text{tip}}}{\omega_{\text{tip}}}\left[\sin(\omega_{\text{tip}}t+\phi_{\text{tip}})-\sin(\omega_{\text{tip}}\tau+\phi_{\text{tip}})\right]}. \tag{S.54}$$

By substituting Eq. (S.54) into Eq. (S.47), we know that

$$\begin{aligned} \alpha(t) &= \int_0^t Q(\tau)e^{-\int_\tau^t P(\theta)d\theta}d\tau \\ &\approx i\sqrt{\gamma_{\text{ext}}}\varepsilon_d\eta_{\text{enh}}e^{-(\gamma+i\Delta)t}\left[1-\frac{ig_xA_{\text{tip}}}{2\omega_{\text{tip}}}e^{i(\omega_{\text{tip}}t+\phi_{\text{tip}})}\right]\int_0^t e^{(\gamma+i\Delta)\tau}\left[1+\frac{ig_xA_{\text{tip}}}{2\omega_{\text{tip}}}e^{i(\omega_{\text{tip}}\tau+\phi_{\text{tip}})}\right]d\tau \\ &\approx \eta_{\text{enh}}\frac{i\sqrt{\gamma_{\text{ext}}}\varepsilon_d}{\gamma+i\Delta}\left[1-\frac{ig_xA_{\text{tip}}}{2\omega_{\text{tip}}}e^{i(\omega_{\text{tip}}t+\phi_{\text{tip}})}\right]\left[1-e^{-(\gamma+i\Delta)t}\right]. \end{aligned} \tag{S.55}$$

From Eq. (S.55), we know that the following term is the corresponding response term of the optomechanical resonator for the motion of the cantilever tip

$$\eta_{\mathrm{enh}} \frac{\sqrt{\gamma_{\mathrm{ext}}}\varepsilon_d}{\gamma + i\Delta} \frac{g_x A_{\mathrm{tip}}}{2\omega_{\mathrm{tip}}} e^{i\left(\omega_{\mathrm{tip}} t + \phi_{\mathrm{tip}}\right)}. \tag{S.56}$$

From Eqs. (S.53) and (S.56), we can see that the following enhancement factor for the response of the optomechanical resonator to the motion of the cantilever tip is introduced

$$\eta_{\mathrm{enh}} = \exp\left[\pi g_{om}^2 \int_{\omega_{c1}}^{\omega_{c2}} \frac{S_\beta(\omega)}{\omega^2} d\omega \right]. \tag{S.57}$$

References:

[S1] Gan, J.-H., Xiong, H., Si, L.-G., Lü, X.-Y. & Wu, Y. Solitons in optomechanical arrays. *Opt. Lett.* **41**, 2676-2679 (2016).

[S2] Grudinin, I. S., Lee, H., Painter, O. & Vahala, K. J. Phonon laser action in a tunable two-level system. *Phys. Rev. Lett.* **104**, 083901 (2010).

[S3] Jing, H., Ozdemir, S. K., Lü, X.-Y., Zhang, J., Yang, L. & Nori, F. PT-symmetric phonon laser. *Phys. Rev. Lett.* **113**, 053604 (2014).

[S4] Zhang, J., Peng, B., Özdemir, S. K., Pichler, K., Krimer, D. O., G. Zhao, Nori, F., Liu, Y.-X., Rotter, S. & Yang, L. A phonon laser operating at an exceptional point, *Nat. Photon.* **12**, 479-494 (2018).

[S5] Hao, H. Y. & Maris, H. J. Experiments with acoustic solutons in crystalline solids. *Phys. Rev. B* **64**, 064302 (2001).

[S6] Kaajakari, V., Mattila, T., Lipsanen, A. & Oja, A. Nonlinear mechanical effects in silicon longitudinal mode beam resonators. *Sensors and Actuators A: Physical.* **120**, 64-70 (2005).

[S7] Bottman, N. & Deconinck, B. KDV cnoidal waves are spectrally stable. http://citeseerx.ist.psu.edu/viewdoc/download?doi=10.1.1.364.5043&rep=rep1&type=pdf

[S8] Leo, F., Coen, S., Kockaert, P., Gorza, S.-P., Emplit, P. & Haelterman, M. Temporal cavity solitons in one-dimensional Kerr media as bits in an all-optical buffer, Nat. Photonics **4**, 471-476 (2010).

[S9] R. J. LeVeque, On the interaction of nearly equal solitons in the KdV equation, SIAM J. Appl. Math., **47**(2), 254-262 (1987).

[S10] P. Lax, Integrals of nonlinear equation of evolution and solitary waves, Comm. Pure. Appl. Math., **21**, 467-490 (1968).